

Iron Isotope Composition of Particles Produced by UV-Femtosecond Laser Ablation of Natural Oxides, Sulfides, and Carbonates

Francois-Xavier d'Abzac,^{*,†,‡} Brian L. Beard,^{†,‡} Andrew D. Czaja,^{†,‡,§} Hiromi Konishi,^{†,‡,⊥} James J. Schauer,^{||} and Clark M. Johnson^{†,‡}

[†]Department of Geoscience, University of Wisconsin, 1215W Dayton Street, Madison, Wisconsin 53706, United States

[‡]NASA Astrobiology Institute, University of Wisconsin, Madison, Wisconsin, United States

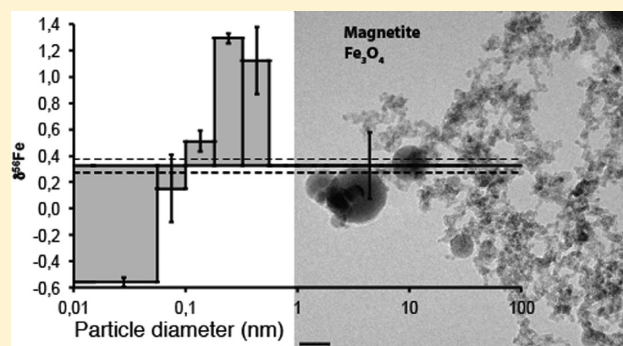
[§]Department of Geology and Department of Chemistry, University of Cincinnati, Cincinnati, Ohio 45221-0013, United States

^{||}148 Water Science and Engineering Laboratory, University of Wisconsin, 660 North Park Street, Madison, Wisconsin 53706-1484, United States

[⊥]Department of Geology, Niigata University, 8050 Ikarashi 2-cho, Nishi-ku, Niigata 950-2181, Japan

Supporting Information

ABSTRACT: The need for femtosecond laser ablation (fs-LA) systems coupled to MC-ICP-MS to accurately perform *in situ* stable isotope analyses remains an open question, because of the lack of knowledge concerning ablation-related isotopic fractionation in this regime. We report the first iron isotope analysis of size-resolved, laser-induced particles of natural magnetite, siderite, pyrrhotite, and pyrite, collected through cascade impaction, followed by analysis by solution nebulization MC-ICP-MS, as well as imaging using electron microscopy. Iron mass distributions are independent of mineralogy, and particle morphology includes both spheres and agglomerates for all ablated phases. X-ray spectroscopy shows elemental fractionation in siderite (C-rich agglomerates) and pyrrhotite/pyrite (S-rich spheres). We find an increase in $^{56}\text{Fe}/^{54}\text{Fe}$ ratios of +2‰, +1.2‰, and +0.8‰ with increasing particle size for magnetite, siderite, and pyrrhotite, respectively. Fe isotope differences in size-sorted aerosols from pyrite ablation are not analytically resolvable. Experimental data are discussed using models of particles generation by Hergenröder and elemental/isotopic fractionation by Richter. We interpret the isotopic fractionation to be related to the iron condensation time scale, dependent on its saturation in the gas phase, as a function of mineral composition. Despite the isotopic variations across aerosol size fractions, total aerosol composition, as calculated from mass balance, confirms that fs-LA produces a stoichiometric sampling in terms of isotopic composition. Specifically, both elemental and isotopic fractionation are produced by particle generation processes and not by femtosecond laser–matter interactions. These results provide critical insights into the analytical requirements for laser-ablation-based stable isotope measurements of high-precision and accuracy in geological samples, including the importance of quantitative aerosol transport to the ICP.



In situ isotopic analyses are critical for documenting spatial heterogeneities within a sample that can be related to petrographic relations among minerals, information that may be critical for complex geological samples. Laser ablation (LA) coupled to mass spectrometry is becoming an increasingly common technique for such measurements.^{3–5} In the case of Fe isotopes, the role that redox reactions have on producing isotopic fractionations has been a major motivation for pursuing isotopic studies of natural samples.^{6,7} Recent work has demonstrated the importance of *in situ* data^{8–10} in interpreting complex samples relative to whole-rock samples that may average isotopic information,¹¹ including studies that have focused on atmospheric evolution during early (Archean) Earth history.¹² Although Secondary Ion Mass Spectrometry (SIMS) is recognized as a powerful *in situ* technique that may

have high spatial resolution down to $\sim 2 \mu\text{m}$,¹³ and precisions for stable isotope measurements of $\sim 0.3\%$ for $^{18}\text{O}/^{16}\text{O}$ ¹³ and $\sim 0.4\%$ for $^{56}\text{Fe}/^{54}\text{Fe}$,¹⁴ recent work has highlighted important accuracy issues related to sample topography and crystal orientation in some high symmetry minerals such as magnetite.^{13,15} In contrast, stable isotope analysis by femtosecond laser ablation is not dependent on such issues and potentially provides more precise and accurate measurements for certain minerals, although the analysis volume is higher than that of SIMS.¹²

Received: August 18, 2013

Accepted: November 22, 2013

Published: November 22, 2013

Despite the promise for LA, challenges remain in determining natural stable isotope variations to a precision and accuracy on the order of a few tenths per mil, a target that is important considering that the natural range in $^{56}\text{Fe}/^{54}\text{Fe}$ ratios is $\sim 5\%$.⁶ For example, Kosler et al.¹⁶ have pointed out that particles created by nanosecond LA may induce artifacts in stable Fe isotope measurements up to 4%. For nanosecond LA, much of this bias reflects thermal-based ablation, and this can be significantly reduced by using femtosecond pulses to remove matter through photomechanical processes not driven by thermal diffusion,^{17,18} potentially obtaining reproducibilities of $\sim 0.1\%$.^{8–10,12} Several important limitations are currently known for femtosecond LA stable isotope analysis. For example, stoichiometric ablation has been a major issue in the search for precision and accuracy of LA-ICP-MS analyses on the elemental scale, and if correction techniques have been developed for this purpose,^{19–21} the question remains opened on the isotopic scale for which deviations of $\sim 0.1\%$ can be significant. Furthermore, Horn and Von Blanckenburg²² reported that inaccuracies could still occur with femtosecond lasers due to incomplete ionization of the largest aerosol particles, and past studies have shown that the largest factors that produce inaccuracies and analytical biases during LA-MC-ICPMS are related to aerosol size, composition, and transport efficiency.²³

In this contribution, we rigorously evaluate the degree of stoichiometric sampling for Fe isotope compositions via femtosecond laser ablation, with the goal of understanding the fundamental processes that lead to Fe isotope fractionation during creation of an aerosol. We use cascade impaction for collecting size-sorted aerosols, followed by conventional solution nebulization Fe isotope analysis. These methods are similar to those that have been used to evaluate stoichiometric sampling of elemental compositions. We demonstrate the control of aerosol size on laser-induced Fe-isotopes fractionation for natural pyrite, pyrrhotite, magnetite, and siderite. The results are discussed from the perspective of particle generation mechanisms associated with femtosecond laser ablation,¹ as well as insights obtained from theory and experiments on elemental and isotopic fractionation during condensation.² We show that this approach allows detection of isotopic discrepancies that are correlated with particle size and matrix, although fs-LA produces stoichiometric sampling of the total aerosol. We conclude that size-dependent stable Fe isotope fractionation produced in a laser-induced plasma plume is dependent on condensation time scales of Fe.

EXPERIMENTAL SECTION

We used an integrated “Analyte-fs” Laser Ablation system (Photon Machines, San Diego, CA, USA) that provides ~ 150 fs pulses at $900 \mu\text{J}/\text{pulse}$ at $\lambda = 266$ nm with an adjustable repetition rate from 1 to 250 Hz. It was operated on raster mode at a speed of $1 \mu\text{m s}^{-1}$, a repetition rate of 25 Hz, a spot size of $12 \mu\text{m}$ using a set of masks, at a fluence of $\sim 1 \text{ J cm}^{-2}$. The ablation cell is a new generation two-volume model (Photon Machines/Cetac “HelEx”)²⁴ that provides a wash out of ~ 0.7 s under a $\sim 0.6 \text{ L min}^{-1}$ flux of helium. The latter is connected to a Micro-orifice Uniform Deposit Impactor (MOUDI).²⁵ The device collects particles as a function of their aerodynamic diameter (d_a) on 12 juxtaposed plates. Argon ($\sim 29.4 \text{ L min}^{-1}$) was added using a “T” connector at the ablation cell output to reach the required 30 L min^{-1} operating conditions of the device.

For solution analyses, PTFE membranes were used as impaction substrates. Their aerosol load was dissolved after collection and processed through anion-exchange chromatography. Iron isotope solution nebulization analyses were conducted on a Micromass “Isoprobe” MC-ICP-MS equipped with a self-aspirating, desolvation nebulizer (Cetac *Aridus II*) operating at $\sim 50 \mu\text{L min}^{-1}$ at the University of Wisconsin, Madison following the methods of Beard et al.²⁶ Data are reported as $\delta^{56}\text{Fe}$ values relative to the average of igneous rocks²⁶ as follows:

$$\delta^{56}\text{Fe} = \left(\frac{^{56}\text{Fe}/^{54}\text{Fe}_{\text{sample}}}{^{56}\text{Fe}/^{54}\text{Fe}_{\text{IGRxs}}} - 1 \right) \times 10^3 \quad (1)$$

On this scale, the IRMM-014 standard has a $\delta^{56}\text{Fe}$ value of -0.09% .²⁷

Aerosols were also collected over separate experiments on polycarbonate membranes (Millipore “Isopore,” $0.2 \mu\text{m}$ porosity) for observation under Scanning and Transmission Electron Microscopes at the University of Wisconsin, Madison. Experimental details are given in the Supporting Information.

Four different minerals were used throughout this study (Table S3), as $>500 \mu\text{m}$ crystal grains mounted on polished sections. Each one was tested for isotopic homogeneity by multiple standard solution analyses using MC-ICP-MS. The magnetite used was collected from the Biwabik iron formation (Minnesota, USA) and is a pure end member (Fe_3O_4) standard that has $\delta^{56}\text{Fe} = 0.32 \pm 0.05\%$. Siderite (FeCO_3) was obtained from a department collection, contains a substantial amount of Mn and Mg, and has $\delta^{56}\text{Fe} = -0.40 \pm 0.07\%$. Pyrrhotite (Fe_4S_5) was purchased from Wards Science (ref # 49-5885) and is a natural specimen from North Bend (Washington, USA); $\delta^{56}\text{Fe} = -0.25 \pm 0.05\%$. Pyrite is a natural, pure end member (FeS_2) from the Balmant mine (New York, USA), and $\delta^{56}\text{Fe} = -1.39 \pm 0.06\%$.

RESULTS

Iron Mass Distribution. Figure 1 shows the IMD for the four studied minerals, including three replicates for pyrite experiments (data available in Table S1 in the Supporting Information). Data are given as percentages of the total

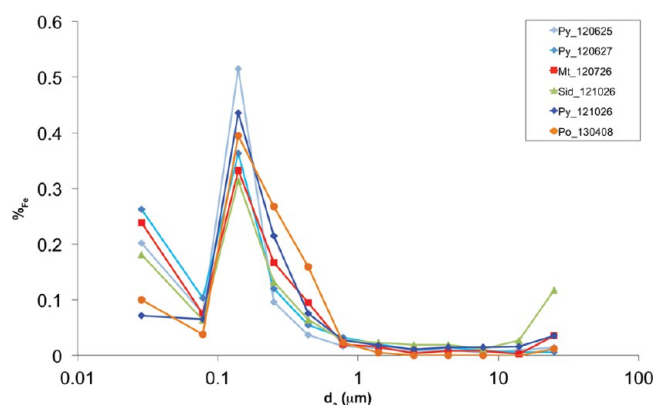


Figure 1. Iron mass distribution of the aerosols collected using the settings reported in Tables S1 and S2. The aerodynamic diameter (d_a) corresponds to the average diameter of the impactor size class (Table S2). The fraction for each size class is expressed as a percentage (%Fe) of the total mass of Fe collected (Table S2). Pyrite (Py, diamonds) experiments were reproduced three times. Other minerals are marked by squares (magnetite “Mt”), triangles (siderite “Sid”), and plain circles (pyrrhotite “Po”).

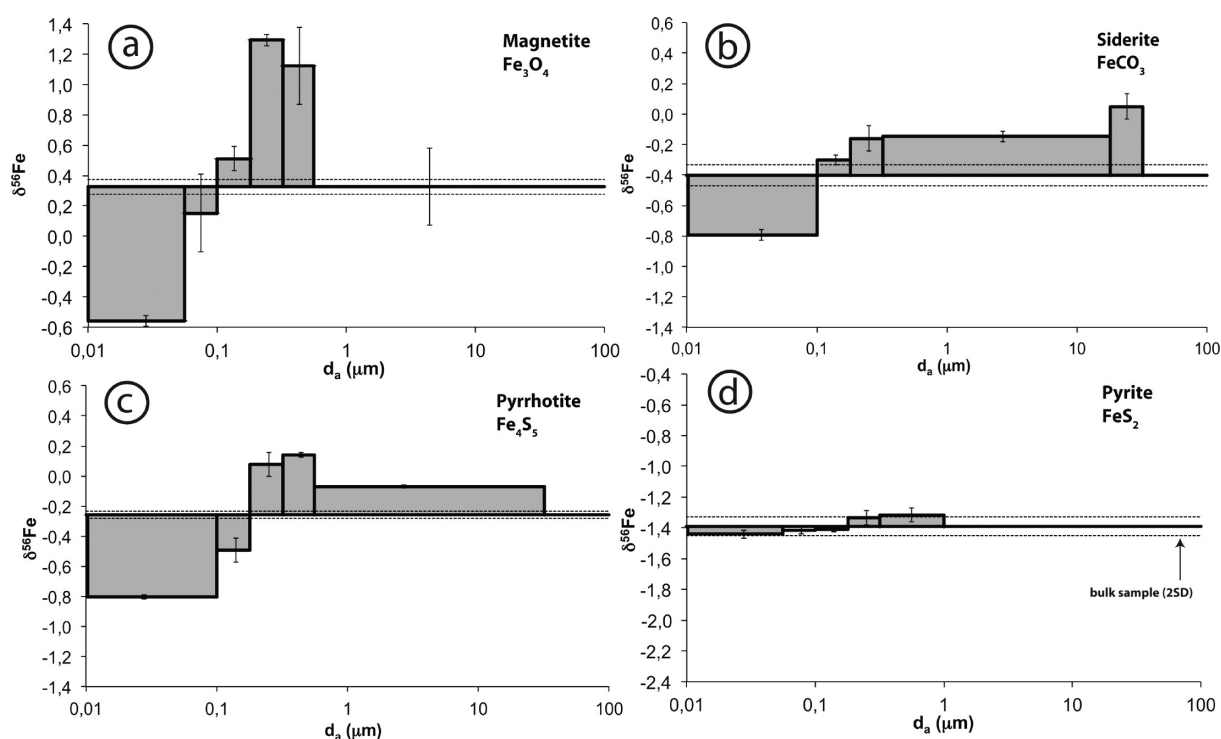


Figure 2. Iron isotope compositions ($\delta^{56}\text{Fe}$) of the size-sorted aerosols collected from magnetite, siderite, pyrrhotite, and pyrite. Histograms are plotted relative to the initial bulk composition (thick line, see “samples” section). Wider sections represent combined samples and are based on the median value of the particle size classes they include. Error bars are 2SD of test solution analyses (see Experimental Section). All numerical data are available in Table S4.

collected Fe mass to allow for comparisons. Similar patterns are observed, with a main peak at $d_a = 0.1 \mu\text{m}$ ($30\% < \%_{\text{Fe}} < 50\%$) and a secondary peak at $d_a = 0.015 \mu\text{m}$ ($7\% < \%_{\text{Fe}} < 26\%$). We detect Fe with siderite for $d_a > 30 \mu\text{m}$ ($\%_{\text{Fe}} = 11\%$), which might be due to the breaking of larger chunks of the crystal under repeated shots,¹⁸ which is likely to happen if the latter presents lattice defects. FEG-SEM observations provided semiquantitative characteristics of each size class population (Figure S3). Agglomerates always outnumber spheres, and the proportion of spheres decreases with size. Finally, when $d_a > 300 \text{ nm}$, no isolated spheres can be found, and the few particles collected are several-micrometer-long agglomerates.

Isotopic Composition of Laser Produced Particles.

The isotopic compositions of the size-sorted aerosols are reported in Figure 2 and Table S4 in the Supporting Information. The histograms are referenced to the initial bulk $\delta^{56}\text{Fe}$ value. Because several size fractions did not contain sufficient Fe for duplicate isotopic analyses, uncertainties correspond to the standard deviation (2SD) obtained on multiple analyses of test solutions that contained similar quantities of Fe. The calculated mass balance Fe isotope compositions match that of the bulk substrate as determined by standard solution nebulization (Table S4) indicating that fs-LA stoichiometrically samples the substrate for Fe isotope compositions.

Individual aerosol particle size groups, however, may have significant Fe isotope heterogeneity. Particles produced by ablation of magnetite show a large range in $\delta^{56}\text{Fe}$ values, increasing from -1% to $+1\%$ between $d_a = 0.015$ and $0.18 \mu\text{m}$, relative to the bulk sample (Figure 2a). For larger particles ($d_a > 0.3 \mu\text{m}$), the inlet to stage 6 had sufficient Fe for an isotopic analysis ($m_{\text{Fe}} > 2 \mu\text{g}$), and its $\delta^{56}\text{Fe}$ value equals that of the bulk mineral. Similarly, siderite shows a significant increase

in $\delta^{56}\text{Fe}$ values from -0.4% to $+0.5\%$ with increasing particle size for the smaller particle populations (Figure 2b). Pyrrhotite shows a similar size– $\delta^{56}\text{Fe}$ relation as seen for magnetite and siderite, where $\delta^{56}\text{Fe}$ values increase from -0.55% to $+0.39\%$ relative to the bulk mineral (Figure 2c) with increasing particle size. In marked contrast, however, pyrite shows minimal size-related isotopic fractionation relative to the bulk sample within uncertainties (Figure 2d, Table S4); this important contrast is discussed in detail below.

Transmission Electron Microscopy. Figure 3 combines TEM bright field (BF) images and EDX spectra on the particles generated from the four minerals studied. All the particles show two types of morphologies: (i) dark, high-contrast spheres with sizes from $\sim 20 \text{ nm}$ to 200 nm and (ii) clear, low-contrast agglomerates of small elements ($< 10 \text{ nm}$), often including spheres.

For magnetite, agglomerates are amorphous and soft-bonded,²⁷ as shown by their chain-like structures. Spheres appear to reflect crystalline material. Energy dispersive X-ray spectroscopy confirms that both types of particles are Fe-rich, and the peak of oxygen could be interpreted to reflect oxygen from the initial sample. However, detected oxygen might also reflect oxidation of the particle surface during aerosol handling and analysis because oxygen peaks also appear with the sulfides. We therefore cannot easily assess changes in Fe enrichment relative to O. Greater confidence, however, may be inferred from Fe/C and Fe/S ratios of different particle size fractions.

Particles from siderite are all crystallized (Figure S4), and agglomerates appear to have a polycrystalline structure, whereas spheres possibly reflect single crystals. The latter are almost depleted in carbon, which indicates that the particles do not reflect a carbonate structure. We define an enrichment factor between agglomerates and spheres as $(\text{Fe}/\text{C})_{\text{agg}}/(\text{Fe}/\text{C})_{\text{sph}}$

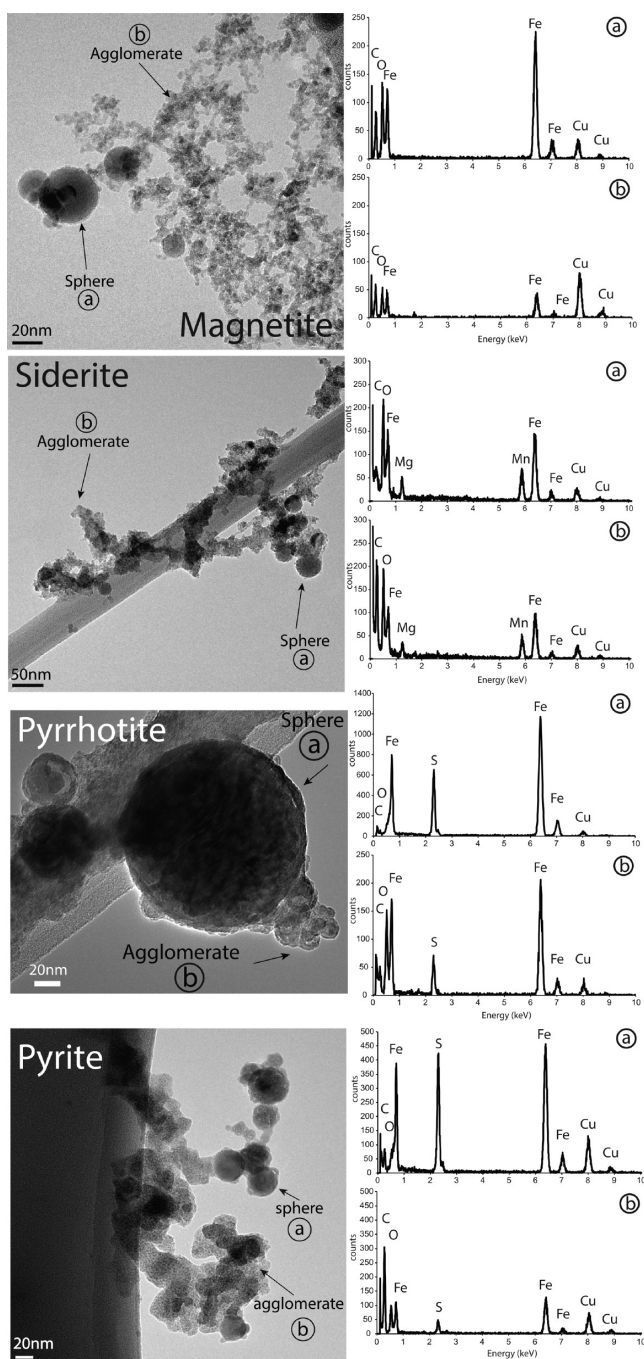


Figure 3. Compilation of Bright Field–High Resolution (BF/HRTEM) images of particles condensed from the different minerals: magnetite, siderite, pyrrhotite, and pyrite. Energy dispersive X-ray spectra correspond to the areas pointed to by arrows. Spheres and agglomerates appear with every ablated mineral, yet agglomerates from magnetite look rather soft bonded compared to the others. Elemental fractionation is observed with siderite (Fe/C), pyrite (Fe/S), and pyrrhotite (Fe/S). The Cu peaks correspond to the TEM grid proximity.

which, on average, is equal to ~ 0.2 , indicating significant Fe–C fractionation. Although some ambiguity in interpreting relative C abundances remains due to possible contamination (membrane, electronic column), this high enrichment in spheres can be related to their growth mechanism, as will be discussed below.

Particles from pyrrhotite are all crystallized (Figure S4 in Supporting Information). Agglomerates are hard-bonded,²⁷ and they appear to blend together better than those from magnetite; this makes the distinction of individual elements difficult for pyrrhotite. The enrichment factor, defined as $(\text{Fe}/\text{S})_{\text{agg}}/(\text{Fe}/\text{S})_{\text{sph}}$ for the sulfides analyzed, reaches ~ 1.5 (agglomerates enriched in Fe by a half). Agglomerates from pyrite are amorphous, and their aspect is similar to pyrrhotite particles. Regular crystalline lattices, as well as multiple crystallized domains in larger spheres, could be observed by selected area diffraction (SAD, Figure S2 in Supporting Information). The enrichment factor for pyrite, calculated in the same way as pyrrhotite, is equal to ~ 2.2 , indicating that agglomerates from pyrite are $\sim 30\%$ more enriched in Fe than agglomerates from pyrrhotite. These results clearly demonstrate Fe–S fractionation among particle species, with distinctly different behavior among the different sulfide minerals studied.

DISCUSSION

Below, we explore the parameters that can explain the different types and degree of isotopic fractionation over the variety of minerals studied. The model proposed by Hergenröder,¹ which notably works out the equations of condensation of Luk'yanchuk et al.,²⁸ is relevant in its description of particle generation mechanisms in a femtosecond laser induced plasma applied to a single element system, following a chronological chain of events. First, the vapor saturation increases until homogeneous nucleation of atomic sized clusters is triggered. It is then quickly released in the vapor phase while the degree of condensation increases continuously and coalescence accelerates the growth of particles. Finally, quenching occurs when the temperature reaches the fusion point.^{28,29} In addition, the simulations and experiments of Richter² provide a useful framework for inferring the specific conditions that may produce elemental and isotopic fractionation, notably during condensation of elements in a cooling system. Quantitative simulations are currently out of reach for multielemental systems such as natural mineral phases because of the large number of parameters that need to be considered. Our interpretation is therefore qualitative and built upon the discontinuous evolution of vapor saturation in the cooling plasma and the triggered continuous condensation. We initially discuss elemental fractionation in our experiments, followed by a focus on the causes of stable Fe isotope fractionations among the various aerosol particle sizes. Finally, we highlight the implications of these results to laser ablation isotopic analyses of geological samples.

Elemental Fractionation. Elemental fractionation is possible under the pressure and temperature conditions of plasmas produced by femtosecond laser ablation,³⁰ and fractionation is primarily controlled by differences in condensation rates.¹ Observations from natural samples led d'Abzac et al.³¹ to develop an interpretative framework of fractionated condensation for elements in the expanding plasma as a function of condensation temperature and saturation vapor pressure. Supersaturation triggers the condensation of elements of different properties (partial pressure, boiling temperature, atomic mass) at different times of the system evolution. Hence, condensation of the most refractory element should start when the material has crossed the melting curve and deviates from the adiabatic expansion path,^{32,33} which probably corresponds to the measured highest atom density peak $\sim 0.5 \mu\text{s}$ after plasma ignition,³⁴ and is followed by coalescence into larger liquid

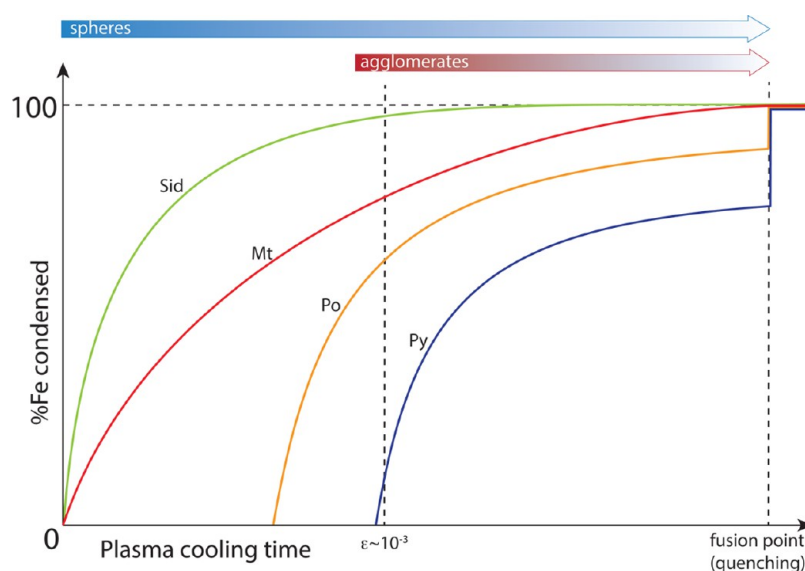


Figure 4. Schematic representation of the amount of Fe condensed (from 0 to 100%) as a function of plasma cooling (from plasma creation at $t = 0$ to time of Fe fusion point) for the four minerals studied. On this time scale, $\epsilon \sim 10^{-3}$ is represented as a late limit for condensation that induces isotopic fractionation (see text). Sphere and agglomerate condensation time scales are represented as blue and red arrows, respectively, on the upper part of the chart. Curve shapes are sketched from the calculations of the degree of condensation in Hergenröder.¹ Iron in magnetite (Mt) condenses from the earliest plasma and reaches 100% near the fusion point. Iron in siderite (Sid) condenses early as well because it is less volatile than C and reaches 100% in a shorter time relative to magnetite. Iron in pyrrhotite condenses even later due to lower saturation for S, and over nearly the same period of time as siderite, based on the similar isotopic fractionation range. Iron in pyrite condenses later than pyrrhotite because of its lower abundance ($\text{Fe}/\text{S} = 0.5$ in pyrite) and its undersaturated state due to an overall decrease in pressure from S condensation; Fe reaches 100% saturation by quenching at the fusion point. This is supported by the hard bonded structure of the agglomerates for these minerals (Figure 3), indicating that small liquid condensates have not acquired a rounded shape before colliding and freezing.²⁷ Iron isotope fractionation in pyrite is therefore reduced to an undetectable level due to the very short Fe condensation time scale (condensation starts near $\epsilon \sim 10^{-3}$), although we would predict substantial S isotope fractionation. The present diagram is an interpretative framework based on experimental results and observations on natural geological samples.

droplets. Supersaturation is then released in the vapor phase.¹ Another element could condense when the vapor becomes supersaturated again during cooling.¹ Small condensates would then be ejected in the plume, quenched upon cooling producing agglomerates. From the present observations, interpreted in the light of the model of d'Abzac et al.,³¹ we propose the following:

(i) For iron oxides, such as magnetite (Figure 3), we assume that Fe has no condensation constraint and hence forms both spheres and agglomerates from the earliest time it is supersaturated in the plasma (Figure 4). Oxygen cannot be properly quantified by EDX, and Fe-bearing particles can easily be oxidized during storage. Hence, eventual Fe speciation into oxides during plasma cooling cannot be assessed. Nevertheless, it is reasonable to think that O forms gaseous species during cooling.

(ii) For siderite, the atomic abundances of Fe and C are equal, but most C is contained in CO_2 with only minor production of C bearing particles.³⁵ Thus, it is believed that Fe condenses first with some C contained in particles that are produced late in the condensation process. This condensation starts before reaching the fusion point because agglomerate morphology indicates that collision was partially occurring in the liquid state²⁷ (Figures 3 and 4).

(iii) For Fe sulfides, the fractionation effects are a strong function of the relative Fe–S abundances of the mineral. In pyrrhotite, because S is lighter and more abundant than Fe ($\text{Fe}/\text{S} = 0.8$), S is likely to start condensing earlier than Fe.¹ However, the lower enrichment factor (~ 1.5) implies that Fe

condensation starts early enough for it to be included into spheres (Figures 3 and 4).

(iv) In pyrite, the much higher S abundance changes the relative condensation time scales relative to pyrrhotite. Although S-rich spheres can be formed in the same way, S is more abundant ($\text{Fe}/\text{S} = 0.5$). The supersaturation drop resulting from the early condensation of S keeps Fe from being saturated in the gas phase until plasma temperature becomes low. Growth of late Fe condensates is then limited, and collision processes dominate to form agglomerates (Figure 4). In this case, this is in agreement with the measured enrichment factor of ~ 2.2 .

Isotopic Fractionation. If the final state of the cooled system was a homogeneous single condensate, there would be no measurable isotopic fractionation since the mass balance between the initial sample and the aerosol is maintained (Figure 2 and Table S4). Moreover, at the extremely high temperatures at which the system evolves (>1000 K), the iron β -factors (i.e., the isotopic fractionation coefficients) tend to zero.³⁶ Here, the $\delta^{56}\text{Fe}$ contrasts between different particle sizes suggest that isotopic fractionation reflects the inability of the condensing matter to homogenize because of plasma expansion and cooling rate and, as such, is a kinetic phenomenon. The former limits particle gathering by pulling them away from each other, the latter of which drives distinct condensation time scales of the different isotopes. This is in agreement with kinetic isotope fractionation observed by Richter,² who modeled kinetic isotope effects relative to condensation time scales and defined a threshold parameter ϵ equal to $\tau_{\text{cond}}/\tau_{\text{T}}$, where τ_{cond} is the condensation time scale of the phase and τ_{T} is the system

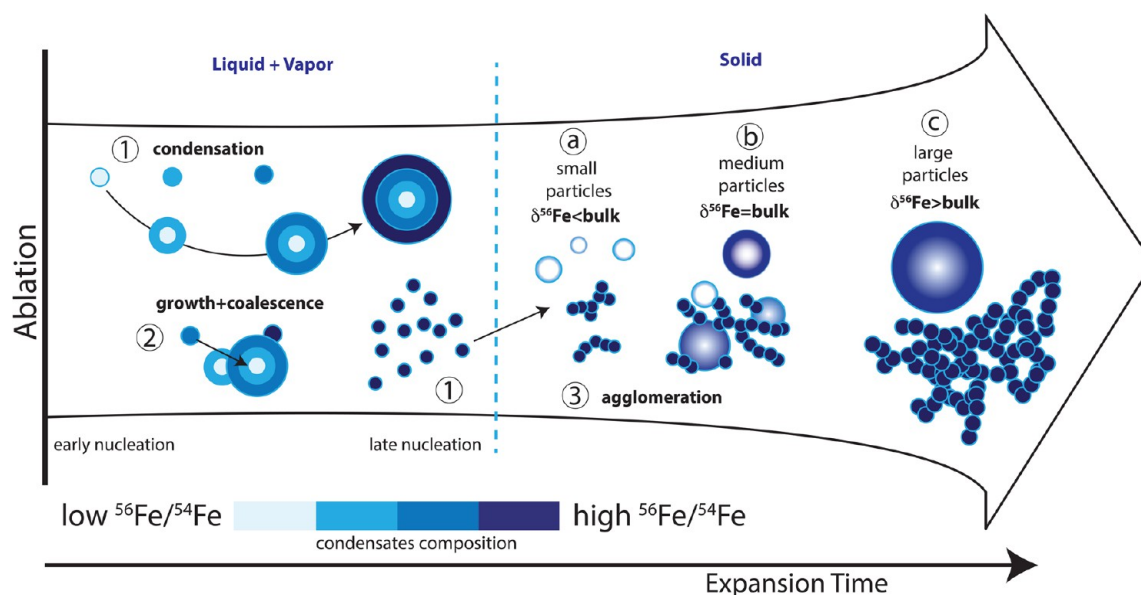


Figure 5. Interpretative framework of Fe isotope fractionation produced in the laser-induced plasma as a function of expansion time (arbitrary scale), based on model of d'Abzac et al.²⁴ Relative enrichment of light Fe isotopes (low $^{56}\text{Fe}/^{54}\text{Fe}$ ratios) is shown in light blue, whereas enrichment in heavy Fe isotopes (high $^{56}\text{Fe}/^{54}\text{Fe}$ ratios) is shown in dark blue (see key). Nucleation, condensation, and particle coalescence (1, 2) occur early in plasma evolution (liquid + vapor state), whereas agglomeration (3) occurs later in the solid state. The range in $\delta^{56}\text{Fe}$ values measured for different particle sizes is illustrated. Small fractions (a) are enriched in small, low- $\delta^{56}\text{Fe}$ spheres and poorly developed aggregates; medium-size fractions (b) have $\delta^{56}\text{Fe}$ values close to the bulk composition, and large-size fractions (c) are composed of highly developed agglomerates and large spheres that have high- $\delta^{56}\text{Fe}$ values.

cooling time scale, which is a constant in the femtosecond regime.³⁰ Kinetic isotope fractionation is likely to occur for $\epsilon > 10^{-3}$ (i.e., for $\tau_{\text{cond}} > 0.1\%$ of the system lifetime).² We consider this parameter relevant for our interpretation because it is (i) dedicated to condensation of multielement materials in the solar system (extreme temperature contrasts and vacuum conditions), (ii) it is defined as a time scale normalized to a system lifetime, i.e., applicable to any condensing closed system, and (iii) it is calculated using various parameters including the cooling rate of the system, the characteristics of the condensates (size, density, number), and the evaporation rate of the condensing elements (Fe in our case). In the Supporting Information, we define these variables, and we develop an approximation of ϵ in the case of Fe condensation from femtosecond laser-induced plasma. We find a similar order of magnitude as that reported by Richter ($\epsilon \geq 10^{-3}$). For comparison, when $\epsilon \sim 10^{-3}$, Richter² predicts a kinetic fractionation for magnesium of $\delta^{25}\text{Mg} \sim -3\%$ within the condensed phase and expects higher fractionation with higher ϵ . On the basis of our observations, we propose the following scenario.

Magnetite (Fe_3O_4). Magnetite is the simplest system of our set of experiments and a good base for the proposed interpretation (Figures 4 and 5). During initial condensation, light Fe isotopes condense more rapidly,² resulting in $^{56}\text{Fe}/^{54}\text{Fe}$ ratios that are lower than those of the bulk sample. These particles gradually acquire later condensates that are enriched in heavier isotopes (high $^{56}\text{Fe}/^{54}\text{Fe}$ ratios) during system evolution (Figure 5-1,2). The last particles to nucleate, therefore, have $^{56}\text{Fe}/^{54}\text{Fe}$ ratios that are higher than those of the bulk solid. This process results in (i) a population of small low- $\delta^{56}\text{Fe}$ spheres which do not grow because of a low coalescence efficiency, as well as poorly developed agglomerates (Figure 5-a), in agreement with the high contrasts of particle density that exist within the plasma between the shockwave

front and the plume tail,^{37,38} which create areas where collision probability becomes very low, (ii) medium-sized particles including a mix of low- $\delta^{56}\text{Fe}$ spheres and high- $\delta^{56}\text{Fe}$ agglomerates (Figure 5-b) that *in toto* have a $\delta^{56}\text{Fe}$ value close to that of the bulk material, and (iii) large spheres that have similar compositions as the bulk sample and large agglomerates that have $\delta^{56}\text{Fe}$ values higher than the bulk (Figure 5-c). Agglomerates have a soft-bonded structure, which suggests they formed during a stage of nucleation²⁷ that is close to the fusion point. Their large numbers would favor collision and agglomeration. As a result, small fractions ($d_a < 50$ nm) are expected to be isotopically light, whereas larger fractions are expected to be progressively enriched in the heavy isotopes (Figure 2-a), reflecting both a higher coalescence level of spheres and a much larger density of agglomerates.

Siderite (FeCO_3). The interpretation made for magnetite is applicable to siderite, because the volatility of Fe is much lower than either O or C. This in turn suggests that during ablation of siderite, Fe should condense early, similar to magnetite. In fact, because, on a molar basis, Fe comprises a smaller proportion in siderite than it does in magnetite, Fe condensation during ablation of siderite should occur on a shorter time scale than it does during ablation of magnetite. This suggests that ablation of siderite will correspond to a lower ϵ , which in turn explains the smaller range in $\delta^{56}\text{Fe}$ values for size-sorted aerosols that was observed in the siderite results, relative to magnetite (Figure 2-b).

Pyrrhotite (Fe_4S_5). For Fe- and S-bearing minerals, S will condense before Fe, although the relative time scales of Fe and S condensation will vary depending upon mineral stoichiometry. For pyrrhotite, which has Fe/S ratios near unity, Fe atomic abundance is high enough so that τ_{cond} is sufficiently long for Fe isotope fractionation to occur (Figure 4). Early homogeneous nucleation of S from the gas phase, a high-energy process, should create surfaces onto which Fe will condense, following a

lower energy path. This effectively shortens τ_{cond} for Fe, thus decreasing the amount of isotopic fractionation that occurs. We suggest this as an explanation for why the aerosol size-sorted range in $\delta^{56}\text{Fe}$ values is not as large as that of magnetite (Figure 2-c), despite a similar Fe abundance.

Pyrite (FeS_2). Pyrite is unique among the minerals studied in that the non-Fe component, S, becomes highly supersaturated earlier than Fe. This contributes to very late Fe condensation, producing very little Fe isotope fractionation in the size-sorted aerosols (Figure 2-d). In the case of ablation of pyrite, the pressure release in the plasma that occurs due to early condensation of S seems likely to be sufficient to maintain Fe below supersaturation³⁹ for an extended time period, and we propose that the delay in Fe supersaturation produces a condition where quantitative rapid condensation occurs as agglomerates late in aerosol evolution, producing no isotopic fractionation as a function of aerosol particle size (Figure 4). This is in agreement with the measured high Fe/S enrichment factor (~ 2.2 ; Figure 3), and the implication is that τ_{cond} is short enough to minimize Fe isotope fractionation despite significant elemental fractionation between Fe and S.²

Implications for LA-MC-ICP-MS. Our results indicate that Fe isotope compositions are stoichiometrically sampled during femtosecond laser ablation of Fe sulfides, oxides, and carbonates (Table S4). Importantly, however, our results highlight that the Fe isotope composition of the aerosol produced by fs-LA is heterogeneous, with the smallest particles tending to have the lowest $^{56}\text{Fe}/^{54}\text{Fe}$ ratios as compared to larger particles that have higher $^{56}\text{Fe}/^{54}\text{Fe}$ ratios, and that the magnitude of this isotopic fractionation is dependent on the substrate. The fractionations that are associated with different substrates are in part controlled by the relative element volatility and abundance in the ablated mineral. This finding brings a new perspective to existing reports on the importance of aerosol transport efficiency,^{16,40,41} and our results demonstrate that it may be critical to ensure that all components and sizes of the aerosol are quantitatively transported to the ICP. Quantitative transport may be ensured, for example, through a reduced transport length.^{42,43} Thereafter, isotopic fractionation may occur downstream, in the ICP, through incomplete ionization of the largest particles²² or by preferential sampling of heavy isotopes by diffusion of the lighter isotopes off the torch axis.⁴⁴ Although these issues are beyond the scope of the present work, complete ionization of particles is likely to occur for small aerosols, and so far, the presently measured IMD appears to be within the range of ionization capabilities of plasma torches;⁴⁵ this is an important component of fs-LA relative to lasers with longer pulse widths.

In addition to highlighting the importance of quantitative aerosol transport, our results raise the issue of matrix matching between sample and standard, especially if transport issues cannot be avoided. From our results, it appears that pyrite is a good candidate for a universal Fe isotope standard because no detectable isotopic fractionation was found during fs-LA, in contrast, for example, to iron oxides, where significant Fe isotope fractionation was measured across the IMD. Looking to other minerals not yet studied, our results suggest that phases which have relatively low Fe contents, notably silicates and nonsideritic carbonates, will also likely have minimal isotopic fractionation across the IMD.

CONCLUSIONS

Isotope ratio analysis that preserves naturally occurring, mass-dependent fractionations provide a rigorous test of analytical biases that may be produced during *in situ* LA-MC-ICP-MS. Here, we isolate the fractionation processes that may occur in the aerosol during UV-femtosecond laser ablation by measuring size-sorted aerosol particles for their Fe isotope compositions using conventional solution nebulization. Particle morphology, IMD, and chemical compositions are in agreement with a multistage mechanism of nucleation, condensation, coalescence, and agglomeration inside the laser-induced expanding plasma. Variable extents of Fe isotope fractionation are observed as a function of particle size, as measured by changes in $^{56}\text{Fe}/^{54}\text{Fe}$ ratios, from 2‰ for magnetite to 0.8‰ for siderite, 1‰ for pyrrhotite, and <0.1‰ for pyrite. Existing models of particle generation inside laser-induced plasmas can explain the measured elemental and isotopic fractionations through differences in the time scales of condensation of Fe relative to other major elements in the oxide, carbonate, and sulfide minerals studied. Elemental fractionation of Fe relative to more volatile elements (C, O, and S) reflects changing supersaturation states, coupled to kinetic Fe isotope fractionations that are most pronounced when the Fe condensation time is long. Magnetite shows the largest Fe isotope fractionation, reflecting early and protracted Fe condensation. Siderite forms aerosols that have smaller extents of Fe isotope fractionation due to the lower amount of Fe (shorter τ_{cond}) relative to other major elements (C and O), as compared to magnetite. With pyrrhotite, early condensed S nuclei provide lower energy pathways and facilitate Fe condensation, producing less Fe isotope fractionation than observed with magnetite and siderite, although still significant, indicating that Fe condensation is not instantaneous. In contrast, the lack of measurable Fe isotope fractionation in size-sorted aerosols produced by fs-LA of pyrite is interpreted to reflect late condensation of Fe; early S condensation releases the Fe supersaturation within the plume, but once the majority of S condenses, condensation of Fe is nearly instantaneous, producing no Fe isotope fractionation. These interpretations provide new insights into understanding the behavior of multielemental systems undergoing condensation from laser-induced plasmas and can help in predicting the extent of isotopic fractionation for a given geological substrate. This work also shows that analytical biases produced by fs-LA do not reflect laser-matter interaction but are produced by variable Fe condensation time scales relative to other matrix elements, recorded in different particle sizes. It is important to stress that the Fe isotope composition of the total aerosol, as reflected in mass-integrated size distributions, is stoichiometric for all minerals studied. These results demonstrate, however, that the isotopic fractionations observed for specific particle sizes during ablation of some minerals requires quantitative transport of the aerosol to the ICP if accurate stable isotope data are to be obtained.

ASSOCIATED CONTENT

Supporting Information

Additional information as noted in the text. This material is available free of charge via the Internet at <http://pubs.acs.org>.

AUTHOR INFORMATION

Corresponding Author

*E-mail: fxdabzac@gmail.com.

Notes

The authors declare no competing financial interest.

ACKNOWLEDGMENTS

Funding was provided by the NASA Astrobiology Institute. FEG/SEM and TEM were performed at the Material Sciences and Engineering Center at UW—Madison. The authors would like to thank Alexander Kvit for his help with TEM observations. John Fournelle is thanked for his assistance with EPMA analyses.

ABBREVIATIONS

IMD Iron mass distribution
PTFE Polytetrafluoroethylene

REFERENCES

- Hergenröder, R. *J. Anal. At. Spectrom.* **2006**, *21*, 1016–1026.
- Richter, F. M. *Geochim. Cosmochim. Acta* **2004**, *68*, 4971–4992.
- Chmeleff, J.; Horn, I.; Steinhöfel, G.; von Blanckenburg, F. *Chem. Geol.* **2008**, *249*, 155–166.
- Hirata, T.; Ohno, T. *J. Anal. At. Spectrom.* **2001**, *16*, 487–491.
- Shaheen, M.; Fryer, B. J. *J. Anal. At. Spectrom.* **2010**, *25*, 1006–1013.
- Johnson, C. M.; Beard, B. L.; Roden, E. E. *In Annual Review of Earth and Planetary Sciences*; Annual Reviews: Palo Alto, CA, **2008**; Vol. 36, pp 457–493.
- Rouxel, O.; Bekker, A.; Edwards, K. *Geochim. Cosmochim. Acta* **2005**, *69*, A549–A549.
- Yoshiya, K.; Nishizawa, M.; Sawakia, Y.; Ueno, Y.; Komiya, T.; Yamada, K.; Yoshida, N.; Hirata, T.; Wada, H.; Maruyama, S. *Precambrian Res.* **2012**, *212–213*, 169–193.
- Horn, I.; von Blanckenburg, F.; Schoenberg, R.; Steinhöfel, G.; Markl, G. *Geochim. Cosmochim. Acta* **2006**, *70*, 3677–3688.
- Steinhöfel, G.; Horn, I.; von Blanckenburg, F. *Chem. Geol.* **2009**, *268*, 67–73.
- Czaja, A. D.; Johnson, C. M.; Beard, B. L.; Eigenbrode, J. L.; Freeman, K. H.; Yamaguchi, K. E. *Earth Planet. Sci. Lett.* **2010**, *292*, 170–180.
- Czaja, A. D.; Johnson, C. M.; Beard, B. L.; Roden, E. E.; Li, W.; Moorbath, S. *Earth Planet. Sci. Lett.* **2013**, *363*, 192–203.
- Kita, N. T.; Huberty, J. M.; Kozdon, R.; Beard, B. L.; Valley, J. W. *Surf. Interface Anal.* **2011**, *43*, 427–431.
- Whitehouse, M. J.; Fedo, C. M. *Geology* **2007**, *35*, 719–722.
- Huberty, J. M.; Kita, N. T.; Kozdon, R.; Heck, P. R.; Fournelle, J. H.; Spicuzza, M. J.; Xu, H.; Valley, J. W. *Chem. Geol.* **2010**, *276*, 269–283.
- Kosler, J.; Pedersen, R. B.; Kruber, C.; Sylvester, P. J. *J. Anal. At. Spectrom.* **2005**, *20*, 192–199.
- d'Abzac, F. X.; Seydoux-Guillaume, A. M.; Chmeleff, J.; Datas, L.; Poitrasson, F. *J. Anal. At. Spectrom.* **2012**, *27*, 99–107.
- Seydoux-Guillaume, A. M.; Freydier, R.; Poitrasson, F.; d'Abzac, F. X.; Wirth, R.; Datas, L. *Eur. J. Mineral.* **2010**, *22*, 235–244.
- Liu, C. Y.; Mao, X. L.; Gonzalez, J.; Russo, R. E. *J. Anal. At. Spectrom.* **2005**, *20*, 200–203.
- Koch, J.; Bohlen, A. v.; Hergenröder, R.; Niemax, K. *J. Anal. At. Spectrom.* **2004**, *19*, 267–272.
- Jaworski, R.; Hoffmann, E.; Stephanowitz, H. *Int. J. Mass Spectrom.* **2002**, *219*, 373–379.
- Horn, I.; von Blanckenburg, F. *At. Spectrosc.* **2007**, *62*, 410–422.
- Garcia, C. C.; Lindner, H.; Niemax, K. *Spectrochim. Acta, Part B* **2007**, *62*, 13–19.
- Shuttleworth, S. *Winter Conference on Plasma Spectrochemistry*; Tucson, AZ, January 9–14, 2012.
- Marple, V. A.; Rubow, K. L.; Behm, S. M. *Aerosol Sci. Technol.* **1991**, *14*, 434–446.
- Beard, B. L.; Johnson, C. M.; Skulan, J. M.; Nealson, K. H.; Cox, L.; Sun, H. *Chem. Geol.* **2003**, *195*, 87–117.
- Gonzalez, J. J.; Liu, C.; Wen, S.-B.; Mao, X.; Russo, R. E. *Talanta* **2007**, *73*, 567–576.
- Luk'yanchuk, B. S.; Marine, W.; Anisimov, S. I. *Laser Phys.* **1998**, *8*, 291–302.
- Ullmann, M.; Friedlander, S.; Schmidt-Ott, A. *J. Nanopart. Res.* **2002**, *4*, 499–509.
- Le Drogoff, B.; Margot, J.; Vidal, F.; Laville, S.; Chaker, M.; Sabsabi, M.; Johnston, T. W.; Barthelemy, O. *Plasma Sources Sci. Technol.* **2004**, *13*, 223–230.
- d'Abzac, F. X.; Seydoux-Guillaume, A. M.; Chmeleff, J.; Datas, L.; Poitrasson, F. *J. Anal. At. Spectrom.* **2012**, *27*, 108–119.
- Hergenröder, R. *Spectrochim. Acta, Part B* **2006**, *61*, 284–300.
- Luk'yanchuk, B. S.; Marine, W.; Anisimov, S. I.; Simakina, G. A. *Optoelectronics '99 Integrated Optoelectronic Devices*; International Society for Optics and Photonics: Bellingham, WA, 1999; pp 434–452.
- Laville, S.; Vidal, F.; Johnston, T. W.; Chaker, M.; Le Drogoff, B.; Barthelemy, O.; Margot, J.; Sabsabi, M. *Phys. Plasmas* **2004**, *11*, 2182–2190.
- Frick, D. A.; Gunther, D. *J. Anal. At. Spectrom.* **2012**, *27*, 1294–1303.
- Polyakov, V. D.; Clayton, R. M.; Horita, J.; Mineev, S. D. *Geochim. Cosmochim. Acta* **2007**, *71*, 3833–3846.
- Gacek, S.; Wang, X. *J. Appl. Phys.* **2008**, *104*, 126101–126103.
- Zeng, X.; Mao, X. L.; Greif, R.; Russo, R. E. *Appl. Phys. A: Mater. Sci. Process.* **2005**, *80*, 237–241.
- Hergenröder, R. *J. Anal. At. Spectrom.* **2006c**, *21*, 1016–1026.
- Bleiner, D.; Lienemann, P.; Vonmont, H. *Talanta* **2005**, *65*, 1286–1294.
- Koch, J.; Walle, M.; Dietiker, R.; Gunther, D. *Anal. Chem.* **2008**, *80*, 915–921.
- d'Abzac, F. X.; Seydoux-Guillaume, A. M.; Chmeleff, J.; Datas, L.; Poitrasson, F. *Spectrochim. Acta, Part B* **2011**, *66*, 671–680.
- Garcia, C. C.; Walle, M.; Lindner, H.; Koch, J.; Niemax, K.; Günther, D. *Spectrochim. Acta, Part B* **2008**, *63*, 271–276.
- Flamigni, L.; Koch, J.; GÄ1/4nther, D. *Spectrochim. Acta, Part B* **2012**, *76*, 70–76.
- Kuhn, H.-R.; Guillon, M.; Günther, D. *Anal. Bioanal. Chem.* **2004**, *378*, 1069–1074.
- DeCarlo, P. F.; Slowik, J. G.; Worsnop, D. R.; Davidovits, P.; Jimenez, J. L. *Aerosol Sci. Technol.* **2004**, *38*, 1185–1205.
- Stookey, L. L. *Anal. Chem.* **1970**, *42*, 779.
- Strelow, F. W. E. *Talanta* **1980**, *27*, 727–732.
- Cohen, B. A.; Hewins, R. H. *Geochim. Cosmochim. Acta* **2004**, *68*, 1677–1689.